Three dimensional image correlation from X-Ray computed tomography of solid foam

Stéphane Roux, François Hild, Philippe Viot, Dominique Bernard

Three dimensional image correlation from X-Ray computed tomography of solid foam

Stéphane Roux, François Hild,

Laboratoire de Mécanique et Technologie (LMT-Cachan)

Ecole Normale Supérieure de Cachan / CNRS-UMR 8535 / Université Paris 6

61 Avenue du Président Wilson, F-94235 Cachan Cedex, France.

Philippe Viot

LAMEFIP, ENSAM de Bordeaux,

Esplanade des Arts et Métiers, 33405 Talence Cedex, France.

and

Dominique Bernard

Institut de Chimie de la Matière Condensée de Bordeaux ICMCB,

CNRS/Université Bordeaux I,

87, Av. Dr A.Schweitzer, 33608 PESSAC Cedex, France.

Abstract

A new methodology is proposed to estimate 3D displacement fields from pairs of images obtained from X-Ray Computed Micro Tomography (XCMT). Contrary to local approaches, a global approach is followed herein that evaluates *continuous* displacement fields. Although any displacement basis could be considered, the procedure is specialized to finite element shape functions. The method is illustrated with the analysis of a compression test on a polypropylene solid foam (independently studied in a companion paper). A good stability of the measured displacement field is obtained for cubic element sizes ranging from 16 voxels to 6 voxels.

Key words: Cellular material, digital image correlation, displacement uncertainty, shape function, strain localization

1 Introduction

X-Ray Computed Micro Tomography (XCMT) is a very precious tool to have access to the details of the full microstructure of a material in a non destructive fashion. By reconstruction from 2D pictures, it allows for a 3D visualization of the different phases of a material [1, 2]. By analyzing these 3D reconstructed pictures, one has access, for instance, to microstructural changes during solidification of alloys [3], to microstructural details during sintering of steel powders [4, 5], to damage mechanisms in the bulk of particulate composites [6, 7] or to the structure of cellular materials (either metallic or polymeric foams) and strains [8, 9]. These actual microstructures may be further processed using e.g. finite element tools [10] for additional exploitations.

Composite materials are of particular interest for the above-mentioned type of studies since the combination of different phases and materials calls for modeling tools that account for strain and stress distributions along and close to interfaces and/or interphases. For instance, damage mechanisms (*e.g.,* interface debonding, fiber breakage) were analyzed in fiber-reinforced composites [11]. The load transfer between fibers and matrices in the presence of cracks was also

Email address: `stephane.roux@lmt.ens-cachan.fr` (Stéphane Roux).

investigated, and mechanical properties of interfaces were then identified [12]. The strain field was obtained by X-ray diffraction techniques.

The behavior of composite sandwich panels is often studied since these structures are widely used in transportation industries. Under extreme conditions (*e.g.,* accidents or crashes), these structures are designed to absorb the impact energy to ensure passengers safety. Therefore, the dynamic response of sandwich structures has to be identified at high strain rates. The essential role of the core on the composite response has been demonstrated [13], and the macroscopic mechanical behavior of different types of core (wood, metallic or polymeric foams) has been identified [14]. The behavior of cellular materials generally includes three steps in static or dynamic compression, namely, an elastic response followed by an important deformation of the material with quasi-constant stress due to strain localization, and densification. The classical models, which are used to predict and improve the behavior of these structures under impact, describe the macroscopic response but do not account for strain localization and hence are unable to relate the behavior to the local microstructure [15]. The cellular material under investigation is a multi-scale foam made out of millimetric porous beads (at the meso scale) which themselves consist of closed micro cells. To improve this foam used as core in sandwich panel, it is therefore essential to propose macroscopic constitutive equations that take into account the physical phenomena observed at all scales (macro-, meso- and micro-scales) of the foam structure. A first point of this study is to reveal strain localization at the bead scale from 3D images obtained by XCMT. Second, strain localization within the bead structure is investigated at the microscopic scale. Last, the measurement of the 3D strain field opens the way for a realistic description incorporating microstructural information, and hence in the long term to optimize this microstructure to meet mechanical requirements for best safety performances.

Cellular materials are one of the constituents of shock absorbing composite [14]. In a companion paper [16], the potential of a direct and exhaustive characterization of the microstructure of a multiscale foam after impact loadings is discussed. Morphology of bead wall was shown to reveal buckling phenomena. Moreover, the use of mathematical morphology tools enables for the extraction individual beads, the estimation of their densities and of the bead density distribution compared to volumetric strains. However, for further information on the strain at a finer scale require a different approach.

In the case of structural composites, 2D Digital Image Correlation (2D-DIC) techniques were used (with images obtained by using a CCD camera) to measure strain fields, to study the influence of the fiber orientation on the macroscopic behavior or to reveal strain and damage localization at the finest scales [17, 18, 19, 20]. Few studies have reported detailed investigations of kinematic analyses using 3D pictures. As a complementary analysis, X-ray diffraction may be used to evaluate elastic strains [12]. However, the reconstructed pictures themselves may be used to evaluate displacements. A first technique consists in tracking markers (*e.g.,* particles). Strain uncertainties of the order of 10^{-2} have been reported [21]. When image processing techniques based upon correlation algorithms are used, strain uncertainties of the order of 10^{-3} can be achieved [22, 23]. A major field of application concerns biomechanical studies [24, 25]. Other studies were devoted to micromechanical analyses of strain fields in heterogeneous materials [23, 4]. Cellular materials have also been studied [8, 9], and 2D strain measurements were performed [26].

The final objective of the present study is to improve mechanical models of sandwich structures (with composite face-sheets and foam core) under dynamic loading. In this first step, 3D-DIC and tomographic techniques are applied to better identify the behavior of the foam core and analyze strain localization appearing in cellular materials during impact. This step is achieved by resorting to correlation techniques. Digital image correlation is a technique that consists in measuring displacement fields based on image pairs of the same specimen at different stages of loading [27]. The displacement field is computed so that the image of the strained sample is matched to the reference image when pixel locations are corrected by the displacement field. Very often, surface images are taken so that only the in-plane displacement and strain components can be identified when using one camera (2D-DIC) or 3D displacements and 2D strains of the surface by using stereo-correlation (2.5-DIC). This technique has revealed to be extremely powerful in solid mechanics for different reasons. It is easy to perform with digital cameras that have very good performances and are low cost, it is a non-intrusive and very tolerant technique that does not require heavy specimen preparations, and last it provides a very rich information (*i.e.,* full-fields). Moreover, algorithms have progressed in the recent years, providing today both robust and very accurate tools (displacement uncertainties are of order 10^{-2} pixel or even below). Last, it allows one to bridge the gap between experiments and simulations by using identification techniques that explicitly use full-field data [28] or for validation purposes of numerical codes [29].

As in 2D applications, the most commonly used correlation algorithms consist in matching *locally* small zones of interest in a sequence of pictures to determine local displacement components [30]. The same type of hypotheses are made in three-dimensional algorithms [22, 31, 23, 32]. This study reports on a different algorithm, which has been shown to be more performing in two dimensions when compared to FFT-based algorithms [33, 34], but had never been extended to three dimensions. The basic approach is close in spirit to the two dimensional case. However, specific procedures aim at saving memory storage, which appears today to be the limiting factor, when using conventional PCs. Since 3D images are the result of a computed reconstruction, the image texture, and more generally its quality cannot directly be compared to two-dimensional optical images. Moreover, space dimensionality has an impact on the expected performances. It is therefore important to validate the performance of the algorithm, one of the motivations of the present paper.

The paper is organized as follows. In Section 2, the way the pictures were obtained through scanning in-situ a compressed foam is discussed. The 3D correlation algorithm is introduced in Section 3 to analyze the obtained pictures. A "global" procedure is implemented in which the displacement field is decomposed over a basis made of shape functions of 8-node finite elements. The performance of the algorithm is evaluated in Section 4 by artificially translating the *actual* reference picture of Section 2. In Section 5, first results are discussed when considering a deformed picture. In particular, the heterogeneity of the displacement and strain fields is analyzed.

2 Description of the experimental test

2.1 Material

The material under investigation is a polypropylene foam. It is a multi-scale material made out of millimetric beads that are agglomerated. During processing, the expanded plastic foam beads are injected into a mold where individual beads are fused together under steam heat and pressure to form a medium without inter-bead porosity. Moreover, the beads themselves are cellular structures with closed cells of size ranging from 10 to 60 μm, with a rather homogeneous microstructure, apart from a much denser skin of about 10 μm in thickness, deprived of large bubbles. As the material is formed, the skin of the beads come together and merge to form a large scale cellular structure. The foam structure is therefore made of beads (mesoscale) and cells (microscale).

Microtomographic images presented in this paper have been obtained on the BM05 beam line at the European Synchrotron Radiation Facility (ESRF) in Grenoble (France). The acquired projections are 2048 $\times$ 2048 pixel radiographs, with a pixel corresponding to 4.91 μm. The sample of polypropylene foam is 10 mm in diameter, and the energy of the beam was set to 16 keV. The use of microtomographic techniques needs a specific methodology to measure the state of the foam structure during dynamic loading. The adopted experimental approach consists in carrying out several interrupted impact tests on a same sample using a drop tower, and acquiring a "picture" in between two impact tests [8]. A tomographic measurement of the sample is taken before the first impact and is used as a reference. During each compression, the deformation amplitude is limited to fixed values, namely 1 mm for the first impact, and 2 mm for the following ones. The sample is maintained compressed and replaced in the microtomographic setup for another acquisition. These operations (impact and X-ray scan) are repeated until densification of the foam. The cellular material deformation can then be evaluated from 3D reconstructions at each stage of the dynamic test (Figure 1).

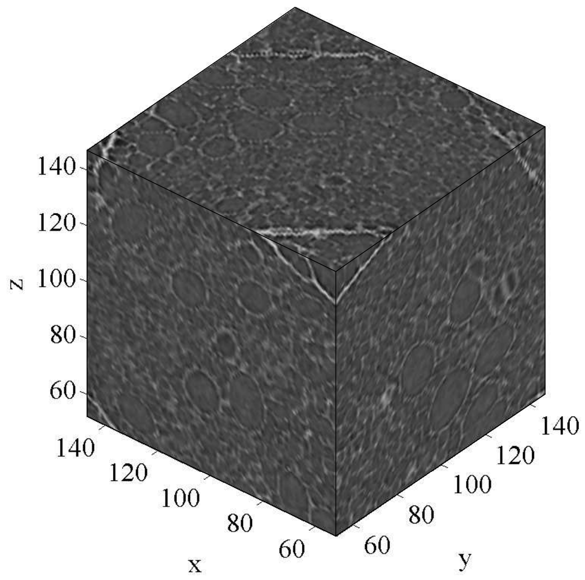

a)

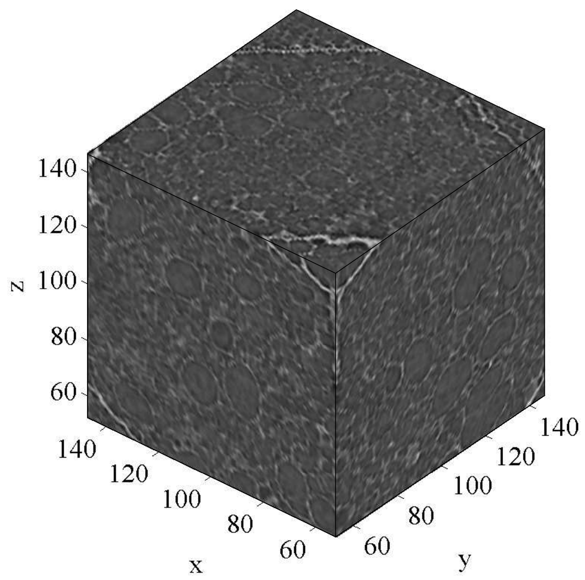

b)

Fig. 1. View of the 96 voxel element volume analyzed in this study (a: reference, b: deformed configurations). A 14-bit deep grey level digitization is used.

2.2 Connection with other related studies

Most studies focused on the influence of the microstructure (*e.g.,* cell shape, size distribution) on the macroscopic behavior of the foam. The influence of the intermediate scale is seldom investigated. However, considering the thickness of bead walls and their relatively high density, it appears necessary to take into account the bead wall rigidity, and further its buckling combined to the cell deformation in order to accurately describe the macroscopic behavior of foams. The microstructure of the material is suitable for the present purpose since it has density contrasts at different scales (from the bubble size to the bead size) that are used here as random "markers" for the correlation algorithm.

Strain fields of the bead (first, along a vertical plane [9] and then in the bulk of the whole sample [16]) have highlighted the physical phenomena of polymeric foam damage under dynamic compression. There are three stages in the deformation of cellular material in compression. First, after a transient elastic phase, stronger bead deformation is located near the compression device surface. In a second phase, observed after the second and third impacts, strains are localized on layers generally perpendicular to the compression direction. Last, densification occurs.

The interrupted impact methodology coupled with micro-tomographic analysis have shown a relationship between bead density and strain level. However, the results show also that the strain heterogeneity is not simply correlated with the density field, namely, the densest beads are not necessarily the least deformed zones. The most porous beads generate randomly located weakness zones in the cellular material that may initiate a local collapse if the neighborhood is favorable, and finally produce a densified layer traversing the entire specimen. It is thus the combined effect of the structure morphology and of the heterogeneous density field that creates a specific strain field for a dynamic compression. There is therefore a need for a complete 3D strain fields to better understand the correlation between the material texture and the way the material deforms.

3 C8 Digital Image Correlation (C8-DIC)

Digital Image Correlation is based on the principle of optical flow conservation [35, 36], namely, the texture of the medium is assumed to be passively advected by the displacement field. If the reference (respectively deformed) image is represented by a three dimensional gray level-valued field, $f(\mathbf{x})$, (respectively $g(\mathbf{x})$), optical flow conservation requires that

$$g(\mathbf{x}) = f(\mathbf{x} + \mathbf{U}(\mathbf{x})) \tag{1}$$

Let us underline that this hypothesis is only an approximation that may be in default in particular for large strains, where the gray value is an integral measure over a voxel size. Moreover, in the case of tomography, a number of artifacts affect the reconstruction, and violate the above hypothesis. However, taking into account a different law, although possible in principle, would require a specific analysis of the bias in the data acquisition technique for the full image, and in the sequel it is assumed that the above hypothesis holds.

In the present study, the general strategy that consists in exploiting cross-correlations between small zones of interest [22, 31, 23, 32] is not used. Rather, an extension to three dimensions of a numerical scheme, which is presented in details for two dimensions in Ref. [33]) is proposed. It is based on a *continuous* and global field as commonly practiced in finite element simulations [37]. It will therefore allow, for example, for *direct and unbiased* comparisons with finite element simulations when the same kinematic hypotheses are made during the measurement and the simulation stages. The basic principles are recalled here, as well as the specific modifications that have been considered for the sake of reducing memory and/or time usage.

The optical flow conservation is considered under the weak form of minimizing the following objective functional $\mathcal{T}$

$$\mathcal{T}(\mathbf{U}) = \iiint_D [g(\mathbf{x}) - f(\mathbf{x} + \mathbf{U}(\mathbf{x}))]^2 \mathrm{d}\mathbf{x} \tag{2}$$

This functional is strongly non-linear and generally displays numerous secondary minima. For computational efficiency, one resorts to a linearized function $\widetilde{\mathcal{T}}$

$$\widetilde{\mathcal{T}}(\mathbf{U}) = \iiint_D [g(\mathbf{x}) - f(\mathbf{x}) - \nabla f(\mathbf{x}).\mathbf{U}(\mathbf{x})]^2 \mathrm{d}\mathbf{x} \tag{3}$$

The way secondary spurious minima are dealt with is two-fold:

- first, the displacement field is searched in a restricted space of functions,
- second, the texture of the images f and g is severely filtered in such a way that the Taylor expansion provides a consistent expression of the texture variation at the scale of the computed displacement.

Once a first determination of the displacement has been computed, the deformed image is corrected by this first determination in order to match the reference one. Because of the filtering, and the restricted nature of the displacement field that is considered, one expects that the displacement field be only a gross approximation of the actual one. However, once the first correction has been performed, the remaining displacement field is likely to be of much smaller amplitude. Consequently, one re-iterates the same procedure, with a less filtered image, and an enriched displacement function basis. This defines one step of an algorithm that may be carried out up to the stage where the unfiltered image is used. In spirit, it is close to multi-grid algorithms used in 2D digital image correlation [38, 33, 39] that allow for the measurement of large deformations.

This general procedure may be applied to a variety of different fields and filters. In the sequel, the considered displacement basis is specialized to be finite element functions over 8-node cubic elements and piecewise tri-linear functions (C8P1 elements). It follows that the algorithm is referred to as C8-DIC. Let us introduce the decomposition

$$\mathbf{U}(\mathbf{x}) = \sum_i a_i \mathbf{N}_i(\mathbf{x}) \tag{4}$$

The minimization of the quadratic functional (3) leads to the following linear system

$$M_{ij} a_j = b_i \tag{5}$$

where

$$\begin{aligned} M_{ij} &= \iiint [\nabla f(\mathbf{x}).\mathbf{N}_i(\mathbf{x})][\nabla f(\mathbf{x}).\mathbf{N}_j(\mathbf{x})]\mathrm{d}\mathbf{x} \\ b_i &= \iiint [\nabla f(\mathbf{x}).\mathbf{N}_i(\mathbf{x})][g(\mathbf{x}) - f(\mathbf{x})]\mathrm{d}\mathbf{x} \end{aligned} \tag{6}$$

Thus a single parameter characterizes the fineness of the displacement basis, namely the size ℓ (in voxels) of the element used. The latter is comparable to the so-called Zone Of Interest (ZOI) size of classical DIC codes.

In so-doing, the displacement field is continuous, and this is an upgrade compared to the procedure used in the early days of 2D digital image correlation [40] where the displacement field was piecewise constant. It was shown in two dimensions that this continuity allowed one to use much smaller zones of interest (typically 8 to 16-pixel as compared to 32-pixel ZOIs [33]). In terms of filters, the most elementary one is used as for the two-dimensional procedure [38], namely, a coarse-graining procedure in which “macro-voxels” are defined to be the sum of $2 \times 2 \times 2$ elementary voxels. The same procedure is used recursively. The main advantage of this procedure is that the volume of images is reduced by a factor of 8 at each coarse-beading stage. Therefore, the first iterations of the procedure have a negligible cost as compared to the final step where the full images are used.

3.1 Differences with respect to 2D implementation

The specificity of three-dimensional images is the large amount of data used in the analysis, and hence the procedure is demanding in terms of memory requirements and computation time. To reduce this over-cost, variations as compared to two-dimensional implementations [33] have been considered:

- Since one generally deals with small strains between consecutive images, one assimilates the reference and deformed coordinate systems, as classically performed in linear elasticity. Therefore, instead of computing the gradient of the original image, a more precise estimate is obtained from the gradient of the average between reference and (corrected) deformed image. However, this amounts to computing all gradients as often as the deformed image is corrected, and from these quantities, estimating the matrix M and second member b, is a rather costly operation. This procedure was not implemented in three dimensions. Rather, the above formulation is implemented directly, and since the reference image f remains invariant, the matrix M is computed once for all at the start of the procedure, and only the second member is corrected.
- The correction process of the deformed image to be performed at each iteration involves a sub-pixel interpolation of the gray levels. In two dimensions, a Fourier transform was used in order to provide a simple interpolation of the data, convenient for translation of zones. However, to limit edge arti-

facts, each zone was initially extended by a frame in which aliasing effects were taken care of through a smooth connection between opposite edges. In the present case, this procedure would be too time consuming, and thus a simple and fast (tri-)linear interpolation of gray levels of the elementary voxel volume containing the required coordinate is implemented.

- The computation of the gradients is performed in two-dimensions through the Fourier interpolation procedure alluded to above. This is important to have consistent gradient and interpolation procedures. In three dimensions, since a linear interpolation is used, a simple finite difference scheme is used.

4 Application to foam tomography

The previously described algorithm is now applied to the three dimensional pictures obtained from XCMT of one bead extracted from a complete specimen. Three states were considered in the experiments. The first one is the reference picture (before any loading). The second is obtained from the sample macroscopically strained at -10% axial compression along the z-axis (just after the first impact). The last one was compressed at -30% mean compression (after the second impact). The strain field of the foam is particularly heterogeneous during the first stage of the dynamic loading. In the companion paper [16], the integral volumetric strain, $\mathrm{tr}(\epsilon)$, at the bead scale was estimated based on a bead wall location technique. Considering only the bead extracted from the sample (labelled “61”, for more details, see Ref. [16]) the average volume change of this bead is respectively -2.7% and -17% for the two studied deformation states. Figure 2 shows three cuts through the same bead studied in this article at the three stages of deformation (macroscopically 0, -10 and -30% strain). One clearly sees in the last stage that the strain is

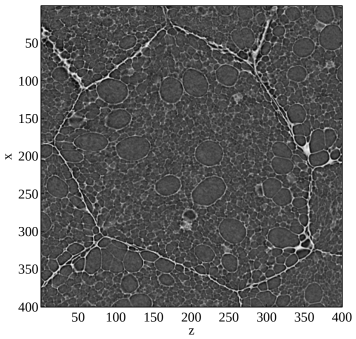

a)

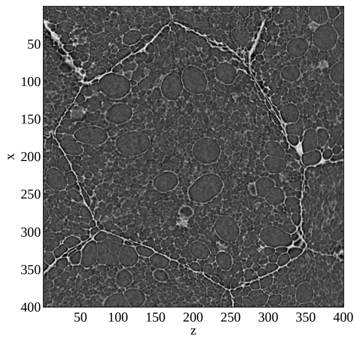

b)

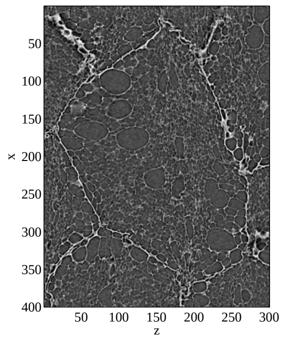

c)

Fig. 2. Cut through the bead “61” in (a) the original state, (b) the −10% compression state, and (c) the −30% compression state. A strain localization is clearly perceptible in image (c), and can be also distinguished in image (b).

such that some cells collapsed. Moreover, one observes that the strain field is very heterogeneous, and a (vertical) compression band may be perceived. At a much more preliminary stage, the same band can already be seen as initiating at the −10% strain stage. Unfortunately, the last pair of images was too much deformed to allow for a satisfactory determination of the displacement. In fact, a good matching of only part of the sample was obtained, and the present localized compression band forbids a global convergence. Thus this last sample will be left aside from the present analysis, and we will only report on the first image pair.

4.1 Image characteristics

Each tomographic image was initially acquired with a resolution of $2048 \times 2048 \times 2200$ voxels whose physical size is 4.91 μm, encoded as 8-bit deep gray levels. This represents a considerable amount of information (*i.e.,* 9.2 Go), which is extremely demanding in terms of memory (storage, RAM and graphic memories). Therefore the entire specimen was not used but rather a specific subset. We focused on a single bead (labelled "61"). The volume containing this bead was already large (*i.e.,* 800^3 voxels). A first data compression was performed reducing the system size by a factor of 4 in each direction. No re-projection of the mean density onto an 8-bit range was performed; the direct sum of the gray levels of the 4^3 block of voxels was assigned to the equivalent macro-voxel. The dynamic range corresponds to 14-bit digitization. The actual dynamic range is of the order of $16,000$, *i.e.,* quite close to the maximum value $(16,384)$. The physical size of those super-voxels is thus four times larger than the original voxel, or 19.7 μm.

Last, in those images, a region of interest (ROI) is defined in which the displacement field will be analyzed. In the following, a cubic ROI of the order of 100 voxels wide in each direction was defined, and centered in the compressed image. The size of the ROI is adjusted to correspond to an integer number of ZOIs (hence typically 104 or 96 voxels). For such sizes, one could deal with ZOIs as small as 5 voxels on a laptop computer (Intel dual core Centrino processor, 2 Go RAM) without encountering memory limitations. For larger ZOIs, *i.e.,* 16-voxel ZOIs, one could reach larger domain sizes (*e.g.,* 176 voxels in each direction). Computation time turned out not to be a limitation factor. A maximum CPU time of the order of 10 min (for ROI sizes of 100 voxels, and a ZOI size of 8 voxels) was sufficient to reach convergence. For a ROI size of 176 voxels, and ZOI size of 16 voxels, the computation time reached about 1 hour.

4.2 A priori performance

Before studying the displacement field between two images, it is important to evaluate the level of uncertainty attached to both the natural texture of the image and the algorithm used. Integer valued displacements do not involve any approximation in the determination of the gray level value. The only difficulty is to be able to capture the displacement without being trapped in secondary minima of the objective function. The most stringent limitation comes from gray value interpolation at non-integer positions. Therefore, in order to assess the uncertainty resulting from this interpolation guess, a uniform displacement of $(0.5, 0.5, 0.5)$ voxel is prescribed on the reference image to produce an artificial "deformed" image. This subvoxel displacement is performed in Fourier space by a phase shift operation. The procedure is then run blindly on this pair of images. The systematic error is measured from the spatial average of the determined displacement. The uncertainty is measured from the standard deviation of the displacement field about its mean value. It turns out that the systematic error is quite small as compared to the uncertainty. Only the latter is reported herein.

The quantification of the uncertainty with respect to the ZOI size is very important because it allows one to determine the optimal ZOI size to be used for a given constraint on the error bars. Large ZOIs will enable one to determine accurate displacements because of the large number of voxels

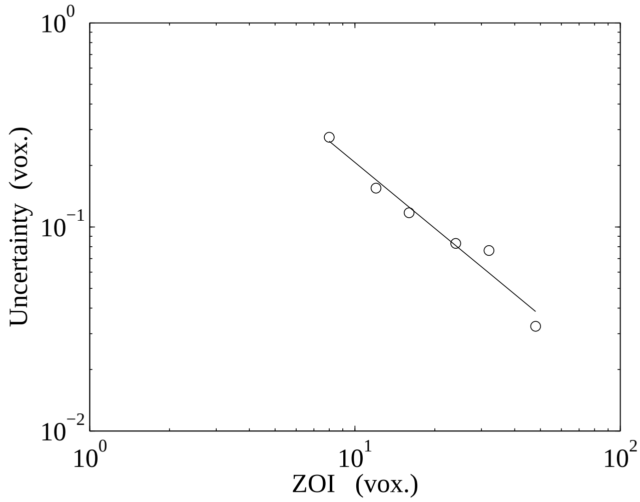

Fig. 3. Log-log plot of the uncertainty in displacement for the artificial case of a uniform translation of 0.5 voxel in each spatial direction, versus ZOI size. Data points are shown as (○) and the straight line is a power-law fit to the data.

involved in each element. Conversely, they are unable to capture complex displacement fields with rapid spatial variations. Conversely, a small ZOI will be flexible enough to follow large displacement gradients, but will give less accurate displacement evaluations.

The uncertainty (here defined by means of the standard deviation $\sigma(U)$ is typically observed in two dimensions to vary as a power-law of the ZOI size, ℓ for FFT-DIC [41] or Q4-DIC [33]

$$\sigma(U) \approx A^{\alpha+1}\ell^{-\alpha} \tag{7}$$

with an exponent α of the order of 1 for FFT-DIC and of order 2 for Q4-DIC and very good textures.

The average uncertainty on the displacement may be estimated to be of order half of $\sigma(U)$ as computed for a displacement of 0.5 voxel in each direction [41, 33]. Figure 3 shows that a reasonable power-law is observed in three dimensions, where a best fit through the data produces the plain line on the graph, with $A = 2.4$ voxels and $\alpha = 1.07$. The prefactor of the mean uncertainty is thus $A/2$, which compares quite well with the corresponding value in two dimensions, where the prefactor is approximately 1 pixel (or $A \approx 2$ voxels). The exponent, α, is a bit disappointing as compared to two dimensional performances. The origin of this small exponent is not yet clear. It may come from the poor approximation used in interpolation and gradients, or be the result of the specific texture of the image. When dealing with more pictures, it will be possible to answer that question.

In order to quantify the strain uncertainty (last column of Table 1), the mean strain is estimated over the entire region of interest for the rigid body translation of 0.5 pixel in each direction. The uncertainty is defined as the *maximum* of the absolute value of the principal strain. As expected, the strain uncertainty decreases with the ZOI size. However, it remains less than 7×10^{-3} for all used ZOI sizes, *i.e.,* small enough to allow us to address the case under study.

5 Results for one loading step

5.1 Matching gap

In order to evaluate quantitatively the difference between two images, a matching gap is defined as

$$R = \frac{\sigma(f - g)}{\max(f) - \min(f)} \tag{8}$$

where σ denotes the root mean square value of the picture difference. It is a dimensionless indicator of the distance between two images, reaching 0 only for identical images. The initial gap between the two images over the region of interest is 9.49 %. The first step, which consists in estimating the mean rigid body translation, reduced the gap to 8.65 %. Good quality optical images are matched up to a final gap of the order of 1 %. In our case, the gray levels should be comparable since, for all images, the same affine transformation to 8-bit conversion is performed after the reconstruction has been performed. Slight difference may however occur due to interferences, (a coherent X-ray beam was used at ESRF) but this may give rise to about 2 gray level variations (or about 1%) in the original images.

In the present case, at convergence, the gap drops to about 5 % between the reference and the corrected image. Table 1 summarizes the final gap for different ZOI sizes. As expected, as the ZOI decreases in size, more and more degrees of freedom are available to reduce the gap. However, the level reached for the smallest ZOI sizes seems to indicate that the incompressible level of mismatch between both images is reached. Although somewhat larger than for two-dimension optical images, the gain with respect to the initial gap is significant enough to indicate that the matching presumably cannot be improved further with the present algorithm.

5.2 ZOI size sensitivity

To check for the stability of the results with respect to the ZOI size, different indicators extracted from the displacement fields are proposed in Table 1. First, the mean displacement estimated from the arithmetic average $\langle \ldots \rangle$ of the nodal displacements, along the three spatial directions, are indicated for ZOI sizes ranging from 16 to 6 voxels. The displacement averages are stable and only fluctuate by about 0.01 voxel (corresponding to 0.197 μm).

Table 1

Influence of the ZOI size on various quantities of interest: mean displacement, matching gap, volume change, axial strain in the compression direction and strain uncertainty.

ZOI size (vox.)	$\langle U_x \rangle$ (vox.)	$\langle U_y \rangle$ (vox.)	$\langle U_z \rangle$ (vox.)	Gap (%)	$\mathrm{tr}(\varepsilon)$ (–)	ε_{zz} (–)	$\delta\epsilon$ (–)
16	−2.28	−0.77	−2.99	5.51	−0.028	−0.038	0.003
12	−2.27	−0.77	−3.00	5.16	−0.028	−0.037	0.004
8	−2.27	−0.77	−2.99	4.88	−0.025	−0.034	0.005
6	−2.27	−0.78	−2.99	4.76	−0.022	−0.032	0.007

To further probe the stability of the displacement results, the mean strain is computed over the entire region of interest. The mean strain is classically defined as the volume (arithmetic) average of the strain. In the chosen discretization, the strain is constant in each element. So that the mean strain is also the average of the strain over elements. In this case, a simple check shows that the inner nodes do not contribute to this estimate and hence only the boundary nodal values matter. However, because these nodes are located on the boundary, they are much less constrained than inner nodes, and hence much susceptible to noise. In order to reduce this spurious effect, the strain estimates are performed by ignoring the outermost elements. One consequence of this however is the fact that the domain over which the strain is estimated is not quite identical when the ZOI size changes. It is observed that the mean volume change, *i.e.,* $\mathrm{div}(\mathbf{U})$, or $\mathrm{tr}(\varepsilon)$, which is a compression of order −2.5% has a tendency to decrease with the ZOI size. However this decrease is only

6×10^{-3} and this estimate of the strain is in agreement with the result obtained by measuring the volume change of iso-surfaces representing the bead 61 (-2.7%, see Ref .[16]). We will see in Section 5.4 that this trend has a simple interpretation. One observes also that the axial strain along the direction of compression follows exactly the same tendency, and hence the transverse area change, $\varepsilon_{xx} + \varepsilon_{yy}$, is approximately constant (fluctuation of the order of 10^{-3}).

5.3 Check of correction from mid-plane cuts

Although it is important to deal with a single number such as the matching gap to evaluate the quality of the displacement determination, a global quantity may hide different types of deviates, from a uniformly distributed difference, to a large but exceptional difference. To have a more faithful appreciation of the quality of the determination, Figures 4, 5 and 6 show three midplane cuts (normal to x, y or z) of the reference image (a), as compared to the as-received deformed image (b), and the corrected deformed image (c) once the determined displacement has been taken into account. Had the determination and image acquisition been perfect, then the section views (a) and (c) would have been identical. Although very significant differences are perceived on the images (a) and (b), the similarity between (a) and (c) is clear.

To further check this similarity, a two-dimensional image correlation analysis (Q4-DIC) was run on the three (a)-(c) pairs. This software is similar in spirit to the one used in three dimensions, and for the image pairs (a)-(c) ideally the displacement field should be zero. It is worth noting that both codes are totally independent, and use some slightly different prescriptions for the

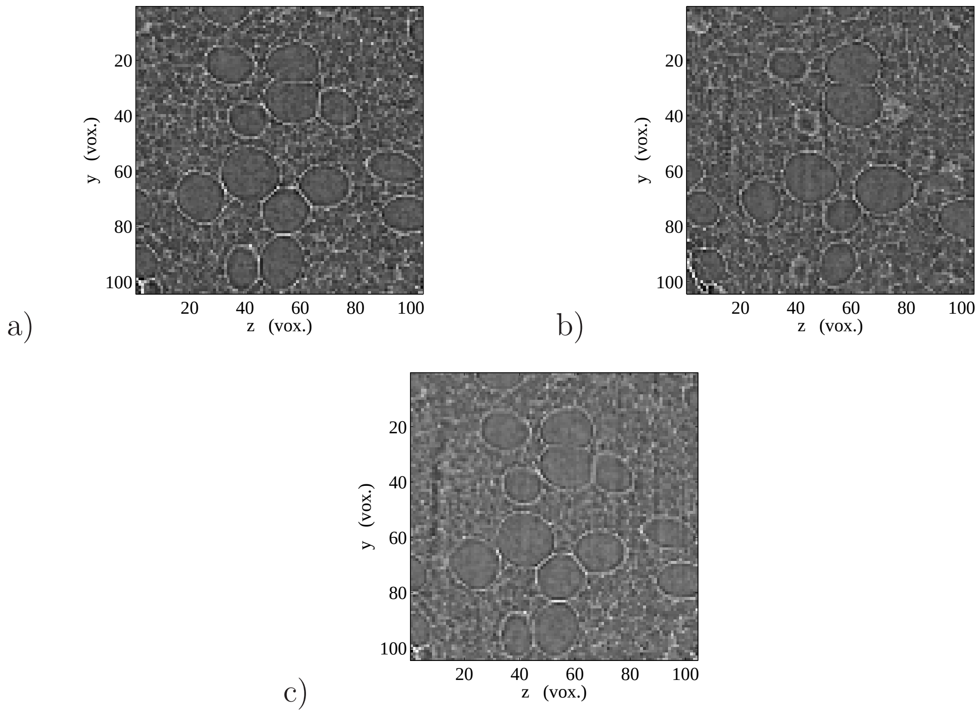

Fig. 4. Reference (a), Deformed (b) and Corrected (c) cut through the specimen for $x = 100$ voxels.

interpolation and gradient computation (as discussed in Section 3.1). This may be responsible for a non-zero answer. The same ZOI size was used as for the three dimensional computation (*i.e.,* 8 pixels). The obtained displacement field was less than 0.02 pixel for all three cuts, and with no visible spatial correlation, (the displacement field seemed similar to white noise). This check is thus considered as an additional validation of the result.

Let us also note that in Figure 4 the deformed image as well as the corrected one display marked vertical lines that seem to be artifacts of the reconstruction. This illustrates the previous discussion on relatively high level of matching gap between images at convergence.

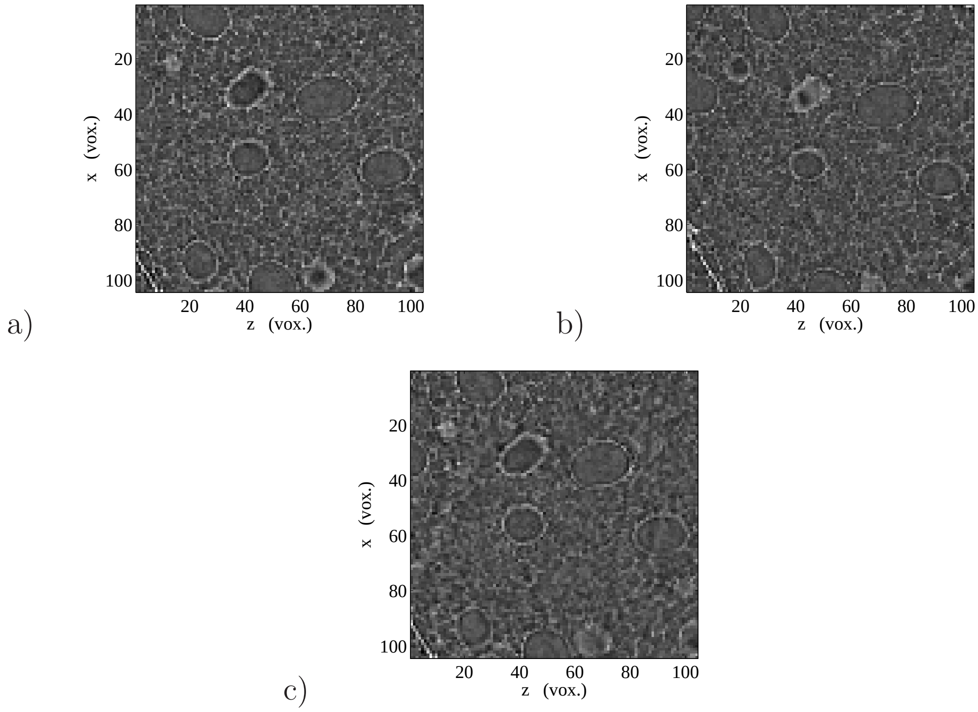

Fig. 5. Reference (a), Deformed (b) and Corrected (c) cut through the specimen for $y = 100$ voxels.

5.4 Influence of ZOI size

One aspect associated with three dimensional analyses of displacements is the fact that it is difficult to visualize three dimensional vector fields. Hence we do not show such graphs. However, to give some indications of the measured displacement field, 2D maps of the component of the displacement field that has the largest mean gradient, namely U_z, along the compression axis is shown. A reference plane corresponding to the mid-plane normal to the x-axis ($x = 100$ voxels) is chosen. Figure 7 shows the corresponding maps of $U_z(x = 100 \text{ voxels}, y, z)$ for four values of the ZOI size, ranging from 16 to 6 voxels in each direction. It is to be noted that the large scale features of the displacement are preserved. It is also observed that small ZOIs are required to capture the sharp gradients, but they unfortunately enhance the noise level

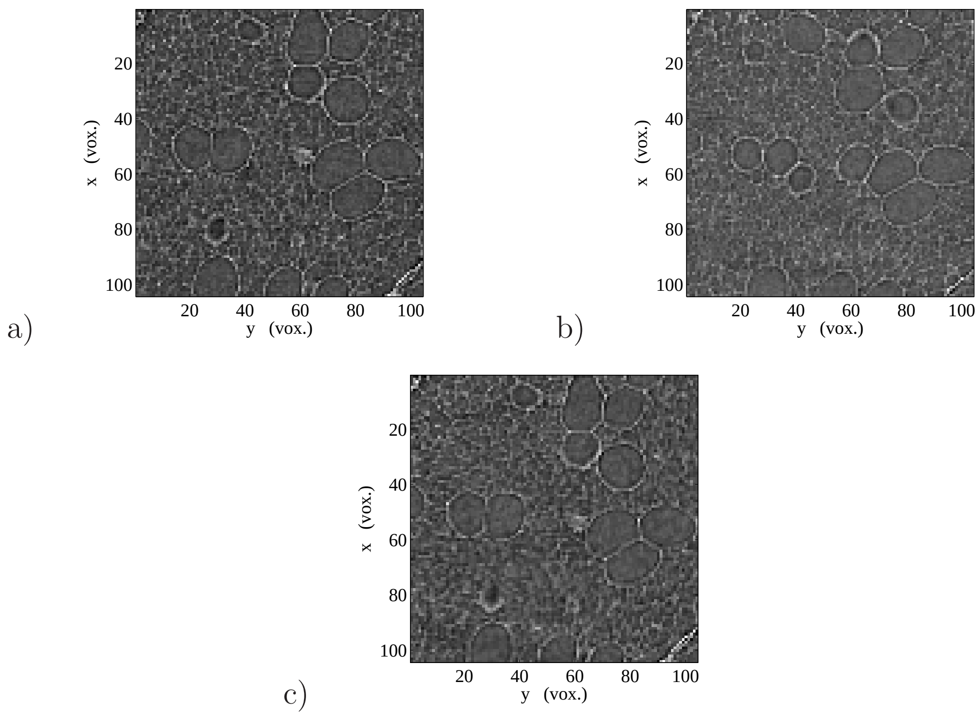

Fig. 6. Reference (a), Deformed (b) and Corrected (c) cut through the specimen for $z = 100$ voxels.

in the displacement measurements.

In order to better illustrate this effect, the corresponding strain maps of the ε_{zz} component are shown in Figure 8. The chosen discretization, C8P1 elements, implies that the strain should be a constant in each element. However, such maps are difficult to compare since the visual impression is limited by the inter-element discontinuities. It was chosen to use a linear interpolation between strains assigned to the center of each element. Let us however note this is a simple rendering effect which does not quite corresponds to the discretization. Note the very large amplitude of the strains distribution shown in this figure, and the consistency between different ZOI sizes. It is obvious that the large ZOI of 16 voxels leads to a diffusion of the strain over large sizes and hence cannot estimate faithfully sudden variations. For sizes of 12 or 8 voxels, two features become well pronounced, namely a compression band located on the

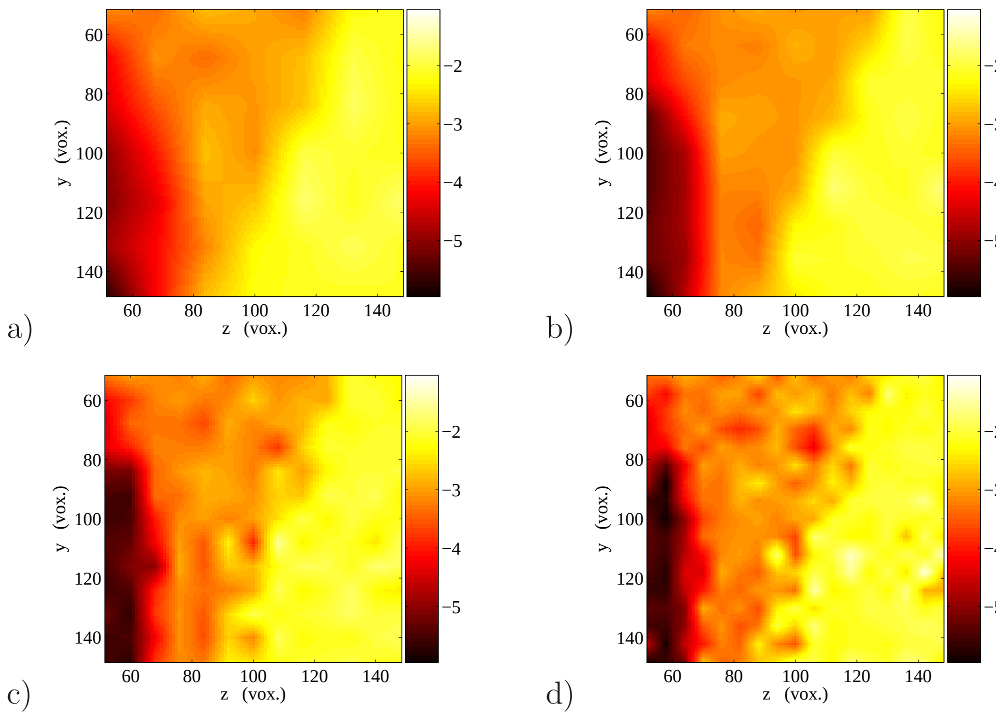

Fig. 7. Comparison between the U_z-component of the displacement field in the $x = 100$ voxels plane, determined using different ZOI sizes a) 16; b) 12; c) 8; d) 6 voxels. The displacement scale is in voxel (1 vox. $= 19.7\mu$m).

left of the domain with strains reaching -25%, and an inclined shear band. For a 6-voxel ZOI, the noise level becomes prohibitive to rely on the quantitative estimates of the strains, but the same features can be seen.

It was previously mentioned that such compression or shear bands could be perceived (qualitatively) between the reference (a) and -10% deformed (b) specimen, and was much more marked for the -30% deformed sample (Figure 2). Cells located on the left side of Fig. (2c) and along a median vertical cut have collapsed. The phenomenon of bead wall buckling can also be seen clearly on these last pictures. It is worth emphasizing that such an abrupt displacement gradient is a very difficult test case where a number of classical two-dimensional image correlation code would fail to detect.

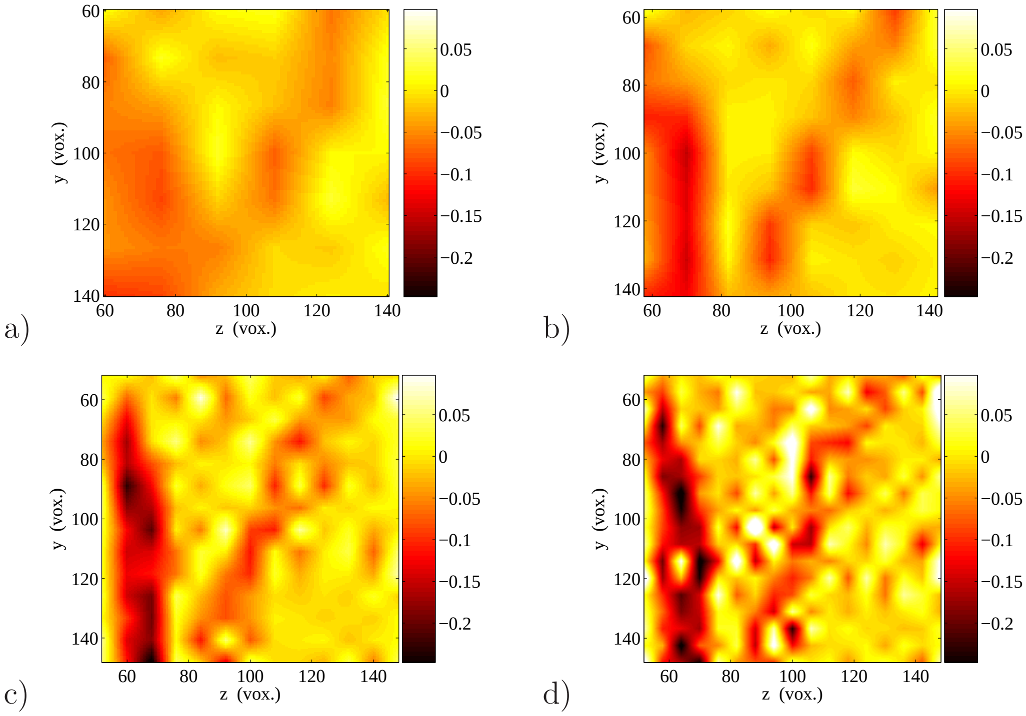

Fig. 8. Comparison between the ε_{zz}-component of the strain field in the $x = 100$ voxels plane, determined using different ZOI sizes a) 16; b) 12; c) 8; d) 6 voxels. In order to decrease the visual impact of the discretization, the maps have been linearly interpolated between element centers where the element strain has been imposed.

The fact that the strains are localized has a direct impact on the evaluation of their mean values. It was mentioned above that the effective size over which the mean strain is computed depends on the ZOI size, because all elements adjacent to the boundary were discarded. If the strain field were homogeneous, this would have no consequence. In the present case however, the opposite assumption that the strain be negligible over the removed element leads to a systematic correction of the order $(1 - 2\ell/L)$ where L is the ROI size. A mean axial strain of order -2.8% *independent* of the ZOI size, is obtained when this first order correction is taken into account.

The amplitude of the displacement is also to be noted, namely, the level spanned by the axial displacement is about 10 voxels, or 530μm, which is already quite large for DIC techniques even if strains were not localized. Let us also observe that as the ZOI size decreases, the displacement field appears to become more noisy. This is an illustration of the uncertainty that increases as the ZOI size decreases, as shown in Fig. 3.

6 Conclusion

A new approach was developed to determine 3D displacement fields based on the comparison of two CT scans. The sought displacement field is decomposed onto a basis of continuous functions using C8P1-shape functions as proposed in classical finite element methods. The latter corresponds to one of the simplest kinematic descriptions. It therefore allows for a *complete* compatibility of the kinematic hypotheses made during the measurement stage and the subsequent identification / validation stages, for instance, by using finite element simulations [10]. Since a linearized functional is considered, a multi-scale algorithm is implemented to allow for small as well as medium range displacements (*i.e.,* at least of the order of the element size).

The performance of the algorithm was tested on a reference image obtained by CT to evaluate the reliability of the estimation, which is shown to allow for either a reasonable accuracy for homogeneous displacement fields, or for a very well resolved displacement field down to element sizes as small as 6 voxels. The displacement field is analyzed on a foam sample where a localization band develops in uniaxial compression. For element sizes ranging from 16 down to 6 voxels, the displacement field is shown to be reliably determined. As far as mean strains are concerned, consistent results were obtained. Strain localization could be observed when analyzing more locally the displacement maps.

The analysis is therefore operational and reliable to deal with CT pictures. However, average strain levels as high as -30% could not be analyzed even with the multi-grid implementation. Scans at intermediate strain levels should have been performed.

The application of this algorithm to study the behavior of cellular materials is encouraging. It has been possible to highlight and identify the heterogeneity of the strain field in a foam. Previous works have shown the heterogeneity of the deformation between beads, at the mesoscopic scale. With this new approach, by combining 3D-DIC and XCMT, the heterogeneity of the strain inside a bead has been shown at a scale close to that of the cell scale. The information will be useful to improve foam models and to better understand the response of this cellular material used in sandwich structures. The phenomena observed and quantified from this method have to be taken into account in a new model. Although these results are very encouraging, in order to follow the entire development of the strain field, it appears necessary to have a more progressive series of image with a more limited displacement difference between successive scans so as to be compatible with the limits of the presented DIC algorithm.

Acknowledgements

This work is part of a project (PHOTOFIT) funded by the Agence Nationale de la Recherche. We acknowledge the European Synchrotron Radiation Facility for provision of synchrotron radiation facilities and we would like to thank Joanna Hoszowska for assistance in using beamline BM05.

References

[1] T. L. Wolfsdorf, W. H. Bender and P. W. Voorhees, The morphology of high volume fraction solid-liquid mixtures: An application of microstructural tomography, *Acta Mater.* **45** [6] (1997) 2279-2295.

[2] J. Baruchel, J.-Y. Buffière, E. Maire, P. Merle and G. Peix, *X-Ray Tomography in Material Sciences*, (Hermes Science, Paris (France), 2000).

[3] O. Ludwig, M. Dimichiel, L. Salvo, M. Suéry and P. Falus, In-situ Three-Dimensional Microstructural Investigation of Solidification of an Al-Cu Alloy by Ultrafast X-ray Microtomography, *Metall. Mat. Trans. A* **36** [6] (2005) 1515-1523.

[4] A. Vagnon, O. Lame, D. Bouvard, M. Di Michiel, D. Bellet and G. Kapelski, Deformation of steel powder compacts during sintering: Correlation between macroscopic measurement and in situ microtomography analysis, *Acta Mater.* **54** [2] (2006) 513-522.

[5] D. Bernard, D. Gendron, J.-M. Heintz, S. Bordere and J. Etorneau, 2005, First direct 3D visualisation of microstructural evolutions during sintering through X-ray computed microtomography, *Acta Mater.*, **53** 121-128.

[6] J.-Y. Buffière, E. Maire, P. Cloetens, G. Lormand and R. Fougères, Characterisation of internal damage in a MMCp using X-ray synchrotron phase contrast microtomography, *Acta Mater.* **47** (1999) 1613-1625.

[7] L. Babout, E. Maire, J.-Y. Buffière and R. Fougères, Characterisation by X-Ray computed tomography of decohesion, porosity growth and coalescence in model metal matrix composites, *Acta Mater.* **49** (2001) 2055-2063.

[8] P. Viot and D. Bernard, Impact test deformations of polypropylene foam samples followed by microtomography, *J. Mater. Sci.* **41** (2006) 1277-

1279.

[9] P. Viot, D. Bernard and E. Plougonven, Phenomenological study of polymeric foam deformation under dynamic loading by the use of microtomographic technique, *J. Mater. Sci.* [in press] (2007).

[10] S. Youssef, E. Maire and R. Gaertner, Finite element modelling of the actual structure of cellular materials determined by X-ray tomography, *Acta Mater.* **53** [3] (2005) 719-730.

[11] M. Preuss, P. J. Withers, E. Maire and J.-Y. Buffière, SiC single fibre full-fragmentation during straining in a Ti6Al4V matrix studied by synchrotron X-rays, *Acta Mater.* **50** [12] (2002) 3177-3192.

[12] R. Sinclair, M. Preuss, E. Maire, J.-Y. Buffière, P. Bowen and P. J. Withers, The effect of fibre fractures in the bridging zone of fatigue cracked Ti6Al4V/SiC fibre composites, *Acta Mater.* **52** [6] (2004) 1423-1438.

[13] H. Mahfuz, T. Thomas, V. Rangari and S. Jeelani, On the dynamic response of sandwich composites and their core materials, *Comp. Sci. and Tech.* **66** [14](2006) 2465-2472.

[14] V.L. Tagarielli, V.S. Deshpande and N.A. Fleck, The dynamic response of composite sandwich beams to transverse impact , *Int. J. Solids Struct.* **44** [7-8] (2007) 2442-2457.

[15] P. Viot, F. Beani and J-L. Lataillade, Polymeric Foam behavior under dynamic compressive loading, *J. of Mat. Sci.* **40** (2005) 5829-5837.

[16] P. Viot and D. Bernard, Microtomography on Polypropylene Foam under Dynamic Loading; 3D Analysis of Bead Morphology Evolution, [submitted for publication] (2007)

[17] S. S. Russell and M. A. Sutton, Strain-field analysis acquired through correlation of X-ray radiographs of a fiber-reinforced composite laminate, *Exp. Mech.* **29** [2] (1989) 237-240.

[18] J. N. Périé, S. Calloch, C. Cluzel and F. Hild, Analysis of a Multiaxial Test on a C/C Composite by Using Digital Image Correlation and a Damage Model, *Exp. Mech.* **42** [3] (2002) 318-328.

[19] M. Muller, E. Toussaint, J.-F. Destrebecq and M. Grédiac, Experimental and numerical study of reinforced concrete specimens strengthened with composite plates, *Comp. Part A* **35** [7-8] (2004) 885-893.

[20] A. Godara and D. Raabe, Influence of fiber orientation on global mechanical behavior and mesoscale strain localization in a short glass-fiber-reinforced epoxy polymer composite during tensile deformation investigated using digital image correlation, *Comp. Sci. Tech.* [in press] (2007).

[21] S. F. Nielsen, H. F. Poulsen, F. Beckmann, C. Thorning and J. A. Wert, Measurements of plastic displacement gradient components in three dimensions using marker particles and synchrotron X-ray absorption microtomography, *Acta Mater.* **51** [8] (2003) 2407-2415.

[22] B. K. Bay, T. S. Smith, D. P. Fyhrie and M. Saad, Digital volume correlation: three-dimensional strain mapping using X-ray tomography, *Exp. Mech.* **39** (1999) 217-226.

[23] M. Bornert, J.-M. Chaix, P. Doumalin, J.-C. Dupré, T. Fournel, D. Jeulin, E. Maire, M. Moreaud and H. Moulinec, Mesure tridimensionnelle de champs cinématiques par imagerie volumique pour l'analyse des matériaux et des structures, *Inst. Mes. Métrol.* **4** (2004) 43-88.

[24] B. K. Bay, Texture correlation: A method for the measurement of detailed strain distributions within trabecular bone, *J. Orthopaedic Res.* **13** [2] (1995) 258-267.

[25] T. O. McKinley and B. K. Bay, Trabecular bone strain changes associated with subchondral stiffening of the proximal tibia, *J. Biomech.* **36** [2] (2003) 155-163.

[26] J. Adrien, E. Maire, N. Gimenez and V. Sauvant-Moynot, Experimental study of the compression behavior of syntactic foams by in situ X-ray tomography, *Acta Mater.* **55** [5] (2007) 1667-1679.

[27] M. A. Sutton, S. R. McNeill, J. D. Helm and Y. J. Chao, Advances in Two-Dimensional and Three-Dimensional Computer Vision, in: *Photomechanics*, P. K. Rastogi, eds., (Springer, Berlin (Germany), 2000), 323-372.

[28] M. Bonnet and A. Constantinescu, Inverse problems in elasticity, *Inverse Problems* **21** (2005) R1-R50.

[29] J. T. Oden, T. Belytschko, I. Babuska and T. J. R. Hughes, Research directions in computational mechanics, *Comp. Meth. Appl. Mech. Eng.* **192** (2003) 913-922.

[30] P. Cheng, M. A. Sutton, H. W. Schreier and S. R. McNeill, Full-field Speckle Pattern Image Correlation with B-Spline Deformation Function, *Exp. Mech.* **42** [3] (2002) 344-352.

[31] T. S. Smith, B. K. Bay and M. M. Rashid, Digital volume correlation including rotational degrees of freedom during minimization, *Exp. Mech.* **42** [3] (2002) 272-278.

[32] E. Verhulp, B. van Rietbergen and R. Huiskes, A three-dimensional digital image correlation technique for strain measurements in microstructures, *J. Biomech.* **37** [9] (2004) 1313-1320.

[33] G. Besnard, F. Hild and S. Roux, "Finite-element" displacement fields analysis from digital images: Application to Portevin-Le Châtelier bands, *Exp. Mech.* **46** (2006) 789-803.

[34] F. Hild and S. Roux, Digital image correlation: from measurement to identification of elastic properties - A review, *Strain* **42** (2006) 69-80.

[35] B. K. P. Horn and B. G. Schunck, Determining optical flow, *Artificial Intelligence* **17** (1981) 185-203.

[36] A. Mitiche and P. Bouthemy, Computation and analysis of image motion: A synopsis of current problems and methods, *Int. J. Comp. Vision.* **19** (1996) 29-55.

[37] O. C. Zienkievicz and R. L. Taylor, *The Finite Element Method*, (McGraw-Hill, London (UK), 4th edition, 1989).

[38] F. Hild, B. Raka, M. Baudequin, S. Roux and F. Cantelaube, Multi-Scale Displacement Field Measurements of Compressed Mineral Wool Samples by Digital Image Correlation, *Appl. Optics* **IP 41** [32] (2002) 6815-6828.

[39] J. Réthoré, F. Hild and S. Roux, Shear-band capturing using a multiscale extended digital image correlation technique, [submitted for publication] (2007).

[40] M. A. Sutton, W. J. Wolters, W. H. Peters, W. F. Ranson and S. R. McNeill, Determination of Displacements Using an Improved Digital Correlation Method, *Im. Vis. Comp.* **1** [3] (1983) 133-139.

[41] S. Bergonnier, F. Hild and S. Roux, Digital image correlation used for mechanical tests on crimped glass wool samples, *J. Strain Analysis* **40** [2] (2005) 185-197.